Science Advances
AAAS

advances.sciencemag.org/cgi/content/full/7/15/eabd1204/DC1

Supplementary Materials for

How Jupiter's unusual magnetospheric topology structures its aurora

Binzheng Zhang*, Peter A. Delamere, Zhonghua Yao*, Bertrand Bonfond, D. Lin, Kareem A. Sorathia, Oliver J. Brambles, William Lotko, Jeff S. Garretson, Viacheslav G. Merkin, Denis Grodent, William R. Dunn, John G. Lyon

*Corresponding author. Email: binzh@hku.hk (B.Z.); zhonghua.yao@uliege.be (Z.Y.)

Published 9 April 2021, *Sci. Adv.* **7**, eabd1204 (2021)
DOI: 10.1126/sciadv.abd1204

This PDF file includes:

H2: Supplementary Materials

A. The global Jovian magnetosphere model

A.1 Implementation of Mass Loading from the Io

The GAMERA code uses a symmetric, eight-cell stencil to reconstruct the numerical fluxes at cell interfaces, which means that the flux through the low-altitude interface depends on the four boundary (ghost) cells as well as the first four active computational cells in the radial direction. Instead of adding a "plasma torus" in the active simulation domain, the mass-loading module directly manipulates the numerical fluxes at the interface of the inner boundary (6 R_j) in order to preserve conservation of mass. This interface flux implementation allows the code to inject the exact amount of heavy (O^+) ions as specified into the active simulation domain. The three-dimensional computational grid is shown in Figure S1. The hard-wall boundary condition keeps plasma populations already in the active domain from leaking back to the ghost zones through the inner boundary (*57*).

The Io plasma torus for mass loading at the inner boundary interface is chosen to be a spatially uniform band centered in the equatorial plane, with ±0.5 R_J extent in the z-direction of the SM coordinates. Figure S2A shows the spatial distributions of the O^+ number density at t = 0.1 (spin), which gives a total rate of approximately 1000 kg/s, within the range of empirical estimations (*33*). The radial momentum flux for O^+ is set to zero, while the tangential momentum fluxes of O^+ are set based on the corotation speed. The energy flux in the mass loading module is then calculated based on a fixed O^+ temperature of 50 eV. Figure S2B- S2C show the corresponding spatial distributions of O^+ number density after the mass loading module switched on for 11 and 22 planetary spins, respectively. It is clear that the spatial distribution of the introduced plasma population exhibits a "torus-like" structure during the whole simulation due to the high resolving power of the numerical schemes used in GAMERA, without significant numerical spreading of the torus plasma in the z-direction. As a key validation of the simulated mass distribution with the Io mass loading, Figure S3 shows the radial profile of the simulated mass of O+ (kg/m), together with the empirical model given by *(33)*. It is clear that the simulated

distribution of O+ mass is in general consistent with the empirical model based on measurements, although in the outer region, the GAMERA simulation underestimates the density, which is possibly due to the lack of hot plasma populations in the MHD simulation.

A.2 Implementation of Magnetosphere-Ionosphere (MI) Coupling and Co-rotation

M-I coupling is implemented by combining Ohm's law with current continuity and the electrostatic approximation in the ionosphere, to obtain the following two-dimensional elliptic equation for the ionospheric electric potential Φ_i, given the field-aligned current $J_{||i}$ at the top of the ionospheric conducting layer (assumed to be $\approx$ 1 R_J and the height-integrated conductance tensor Σ):

$$\nabla \cdot \Sigma \cdot \nabla \Phi_i = J_{||i} \cos\alpha \quad (1)$$

The dip factor cos α is $\boldsymbol{b}\cdot\mathbf{r_0}$, where $\boldsymbol{b}$ is a unit vector pointing along the dipole magnetic field at the top of the ionospheric conducting layer and $\mathbf{r_0}$ is the radial unit vector in spherical polar coordinates. Field-aligned current $J_{||i}$ is computed near the low-altitude computational boundary at approximately 6.1 R_J Jovicentric in the magnetosphere and is then mapped along dipole field lines assuming $J_{||}/B$ = const to the top of the height-integrated ionospheric conducting layer to give $J_{||i}$. The height-integrated substrate is located at 1.01 R_J Jovicentric where equation (1) is solved. The ionospheric electric potential Φ_i obtained from equation (1) is mapped along dipole field lines to the inner computational boundary (6 R_J Jovicentric) assuming the magnetic field lines are equal-potential. The electric field at the boundary is calculated as $\mathbf{E}_\perp = -\nabla_\perp \Phi_i$ which serves as a part of the low-altitude boundary condition for the MHD solver. The ionospheric potential equation is solved with a newly developed code, dubbed REMIX, largely based on the legacy Magnetosphere-Ionosphere Coupler/Solver (MIX) program (*58*). As a first step, we neglect the gradient of the Hall conductance and use Σ_P = 0.1 S as an approximation for the Jovian ionosphere (*59*).

After solving the convective potential Φ_i, the implementation of corotating magnetospheric plasmas and flux tubes is equivalent to adding a tangential electric field component at the inner boundary of the simulation domain induced by the rotation of the Jupiter:

$$E_{cr} = -(\boldsymbol{\Omega}_J \times \mathbf{r}) \times \mathbf{B}, \quad (2)$$

where $\Omega_J = 1.76 \times 10^{-4}$ rad $\cdot$ s^{-1} is the angular speed of Jupiter's rotation, corresponding to a 9.9 hours period. At Jupiter's ionospheric reference altitude ($\approx$ R_J) with equatorial magnetic field strength B_J, the corotation of the Jovian magnetosphere is implemented by imposing a time-stationary corotation potential Φ_{coro} at the ionospheric boundary given by:

$$\Phi_{coro} = -\Omega_J B_J R_J^2 \sin(\lambda), \quad (3)$$

where λ is the magnetic co-latitude, B_J = 4.27 G, R_J = 69911 km. This corotation potential is combined with the electrostatic potential Φ_i solved through Equation (1) in the REMIX module and dipole mapped to the inner boundary of the MHD domain:

$$\Phi_{total} = \Phi_i + \Phi_{coro}. \quad (4)$$

Then the electric field driving the corotation at the inner boundary is calculated as $E = -\nabla\Phi$ total. Figure S3 shows the spatial distribution of the time-stationary Φ_{coro} and a snapshot of Φ_i at t = 203.5 hour at the interface of the inner boundary (6 R_J). Note that the peak value of Φ_{coro} is -70967 kV, while the peak value of Φ_i is only -643 kV, suggesting that the ionospheric "convection" potential is in general much smaller than the corotation potential, which is consistent with previous estimations (*60*). The value of Φ_i is consistent with the magnetopause reconnection potential, which is approximately 586 kV calculated based on the instantaneous electric and magnetic fields.

Above 83 degrees MLAT, the peak corotation potential is approximately 6200 kV, which is still about one order of magnitude greater than the convection potential. The comparison between the corotation potential Φ_{coro} and the ionospheric convection potential Φ_i shows that the Jovian magnetosphere is largely driven by the rotation of the planet, and the solar wind-magnetosphere interaction may be a secondary effect when driven by nominal upstream conditions. In the simulation driven by steady state east-west IMF conditions, the location of the upward field-aligned current, which may be related to the invert-V type of electron precipitation, is related to the amount of mass loading and planetary rotation. In the numerical experiment shown in this study, the location where the rotation speed drops down to 70% of the local corotation speed, is a function of local time and is around 30-35 Rj on average, which is consistent with theoretical estimations (*13*).

B. Determination of the reconnection separatrix

B.1 The hemispheric-marching method

Magnetic reconnection occurs on the magnetopause where the incoming IMF have a sufficient shear angle relative to the intrinsic magnetic field line of the planetary magnetosphere. The reconnected field lines become open which end in the low altitude boundaries of the southern and northern hemisphere, respectively. A "reconnection site" at which reconnection takes place is surrounded by four magnetic topologies: IMF, closed, open in the south, and open in the north. A "reconnection separatrix" is then generated by connecting all the reconnection sites identified based on the field topology.

In the Jovian magnetosphere under steady-state IMF driving without considering the effect of dipole tilt, the reconnection separatrix is a continuous curve along the magnetopause, tilted from the equatorial plane. In general, the orientation of the separatrix is dependent on the IMF clock angle, and the angle of the reconnection separatrix relative to the dipole moment, i.e., the positive *z*-axis in the case of Earth, is half of the IMF clock angle θ defined as $\text{atan}(B_z/B_y)$ (*34*).

We use a hemisphere-marching method to identify the reconnection separatrix on the simulated Jovian magnetopause (*61*).The algorithm starts from one magnetic null point and ends in the other null point on the other side of the noon-midnight meridional plane. Note that while the searching for magnetic null point is not an easy task especially under dynamic IMF conditions, we found that except for parallel (southward) IMF driving, the Jovian reconnection separatrix crosses the vicinity of the subsolar point regardless of the IMF clock angle θ.

In the separatrix-tracing algorithm, the starting point is selected on the last closed field line that intersects with the equatorial plane at 12 magnetic local time (MLT). Centered at the starting point, a dawnward-facing hemispheric surface with a radius of 5 R_J is sliced into a 60×60 longitude-latitude mesh. Magnetic field lines are traced starting from these 3600 grid points to determine the distribution of magnetic topology surrounding the starting point. The one-sided hemisphere mesh is chosen such that it guarantees to sample both the magnetosphere and the magnetosheath. Based on the magnetic field topology, one block with northern hemispheric open field line connections and another block with southern hemispheric open field line connections can be identified on the hemisphere surface. The midpoint of the two points from the two blocks is regarded as a point right on the reconnection separatrix. This midpoint is used as the center of the next hemispheric surface, on which the identification process is repeated. The hemispheric surface marches along the magnetopause toward the dawnside until one or both of the open topology blocks vanishes. A duskward-facing hemispheric surface is then created for the duskward marching, which is complimentary to the first hemispheric surface in the dawnward marching.

Figure S4 shows the reconnection separatrix along the magnetopause traced using the hemisphere-marching technique. It should be pointed out that the separatrix is not in the equatorial

plane since the IMF deviates from the east-west orientation. The reconnection potential is calculated by integrating the parallel component of the electric field $\boldsymbol{E}_{\parallel}$ along the reconnection separatrix. Using the average electric and magnetic field calculated between Spin 21-23, the integral method gives approximately 508 kV as the reconnection potential on the dayside magnetopause.

B.2 Possible influence of hot plasma populations

The current global simulation of the Jovian magnetosphere lacks a non-thermal (hot) plasma population in the outer magnetosphere, which is unlikely described by resistive MHD. Thus, the simulated stand-off distance of the Jovian magnetosphere ($\approx 50\ R_J$) is lower than values from in-situ observations ($> 60\ R_J$), which is determined by the balance between the SW dynamic pressure and the magnetic pressure of the Jovian dayside magnetosphere. The implementation of such a non-thermal, hot plasma population requires including non-MHD physical treatment, which is yet to be developed and has not been implemented in any of the current numerical simulations of the global Jovian magnetosphere. The underlying physical processes and numerical experiments on adding the non-thermal plasma population in the outer Jovian magnetosphere is a separate topic, which will be investigated in follow-up studies. Here we discuss briefly the possible influences of the missing hot population on the dayside SW-Magnetosphere interaction based on the balance of magnetosheath forces (*62*).

If a hot plasma population is included in the simulation, the size of the jovian magnetopause increases with a greater stand-off distance and a blunter-shaped magnetopause due to the increased total pressure in the outer jovian magnetosphere. If the width of the magnetosheath did not change with the inflated magnetosphere (*55*), the Jovi-effective length in the dayside solar wind is expected to increase proportionally as the size of the magnetosphere, resulting in an increase of approximately 15−20% in the dayside merging potential. However, since the width of the magnetosheath is also proportional to the size of the magnetosphere, the increase in the magnetosheath width diverts more solar wind flux, resulting in a decrease in the dayside merging potential (*63-65*). On the other hand, numerical experiments have shown that a blunter magnetosphere causes additional diversion of the solar wind flux tubes, which further suspends the merging of solar wind flux. As a consequence, the 15 − 20% enhancement in the dayside merging potential is possibly an overestimation of the effect from including a hot population. Thus, although the hot plasma population has potentially a significant effect on the size of the simulated Jovian magnetosphere, its quantitative influence on the dayside merging between the SW and the Jovian magnetosphere is possibly less than 10%. Future studies are needed to provide more accurate estimations.

C. Instantaneous Magnetic Field Topology

Figure S6 shows the simulated magnetic field topology at the four snapshots shown in Figure 3 of the manuscript. It is clear that although the instantaneous field lines are more complicated (less smooth) compared to the average field directions, the main parts are consistent – e.g., a closed polar cap as shown by the black field lines in the plots. Therefore, although the simulated magnetic field topology is highly dynamic, yet it is a relative robust feature of the simulation, especially in the polar region where most of the field lines are closed flux tubes at different rotation phase.

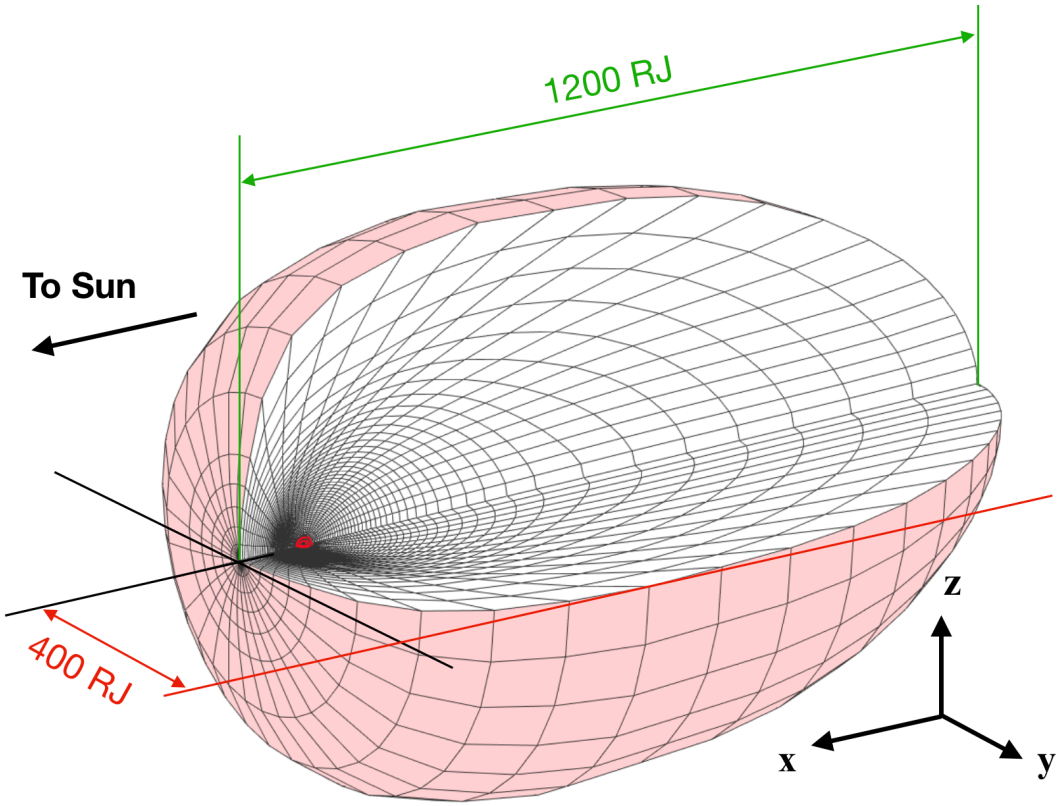

Fig. S1. The 3-D view of the stretched spherical grid. The distributions of the grid cells are shown in the equatorial and meridional planes. The grid resolution showing contains 64×64×64 computation cells while the actual calculation uses 256×256×256 (radial×meridional× azimuthal) cells in the spherical coordinates.

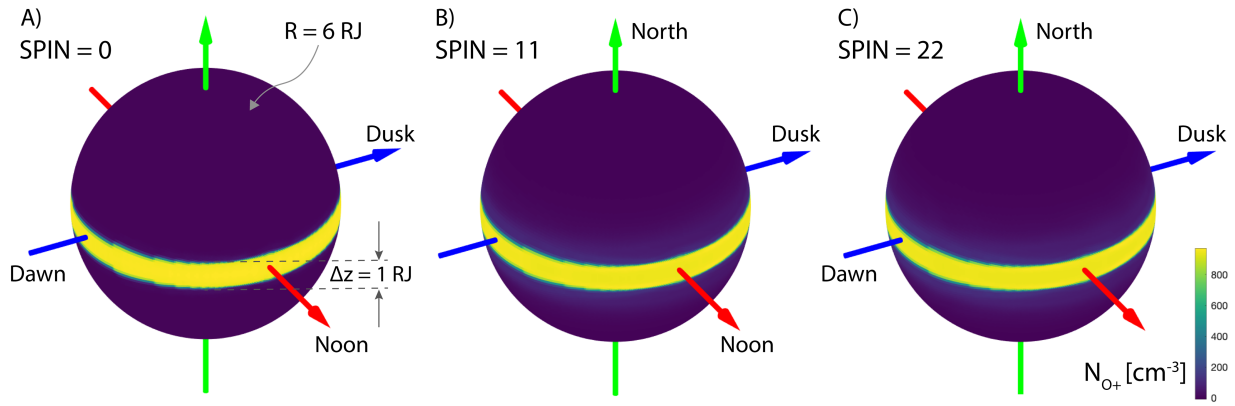

Fig. S2. The spatial distribution of Io number density at the low-altitude (6 R_J) boundary of the simulation domain. A) t=0; B) t = 100 hour (spin 11) and C) t = 200 hour (spin 22)

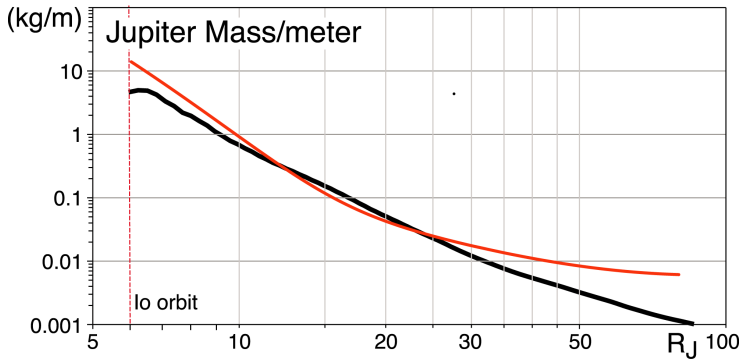

Fig. S3. **Average radial distribution of mass per meter calculated in the simulation**. The black curve is derived from the simulation, compared with the red curve from empirical results in *(33)*.

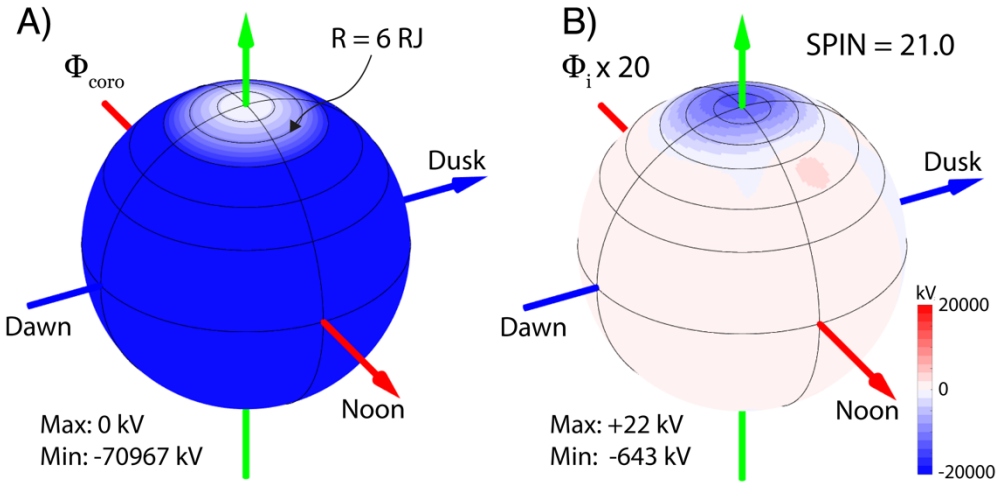

Fig. S4. The A) corotation potential versus B) convection potential at t = 203.5 hour.

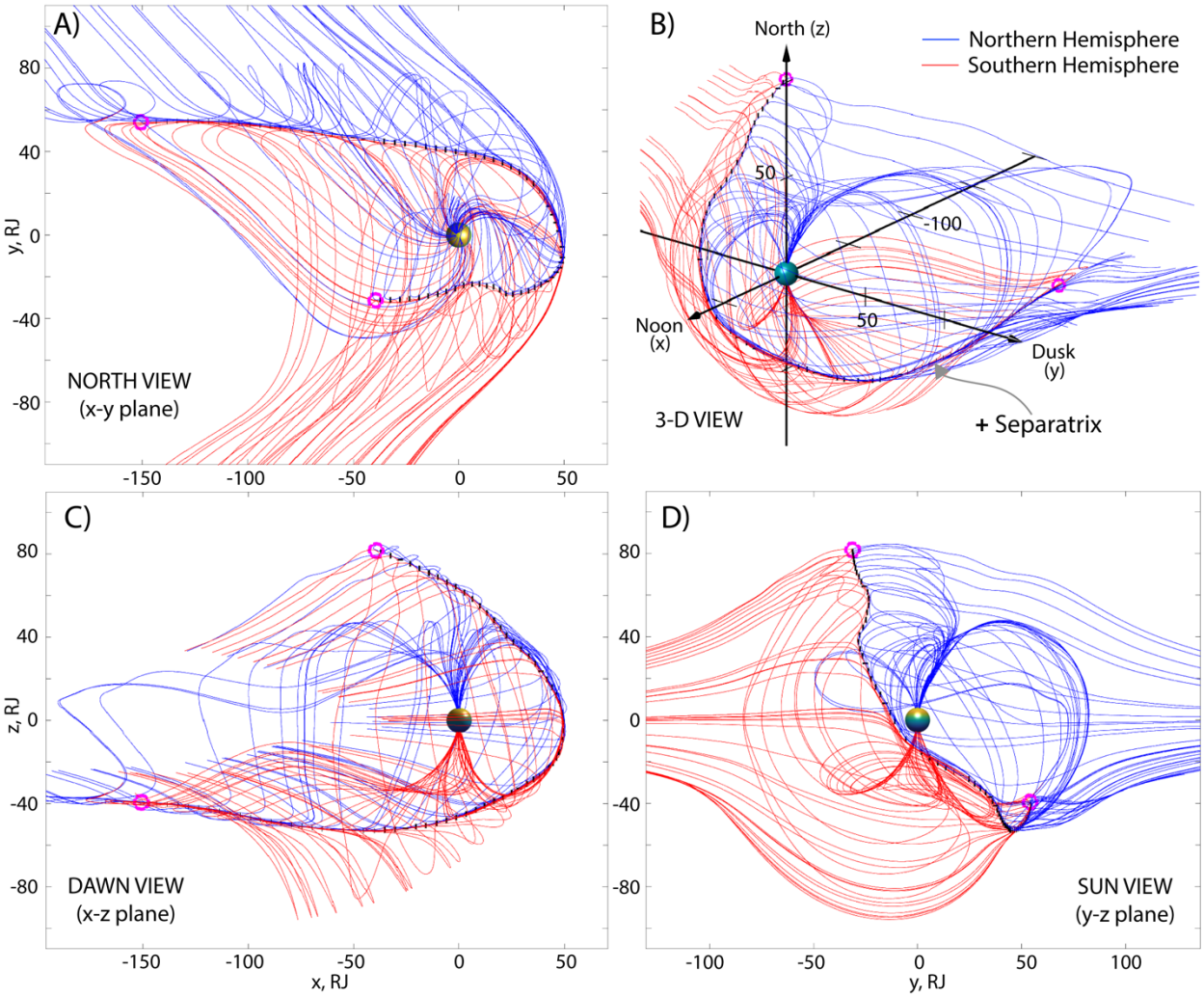

Figure. S5. The magnetic reconnection separatrix (black). Viewing from the A) north, C) the dawnside, and D) the Sun. The corresponding three-dimensional view is shown in panel B). The blue (red) field lines have ionospheric footprints in the northern (southern) hemisphere. The magenta points indicate the terminations of the magnetopause reconnection separatrix.

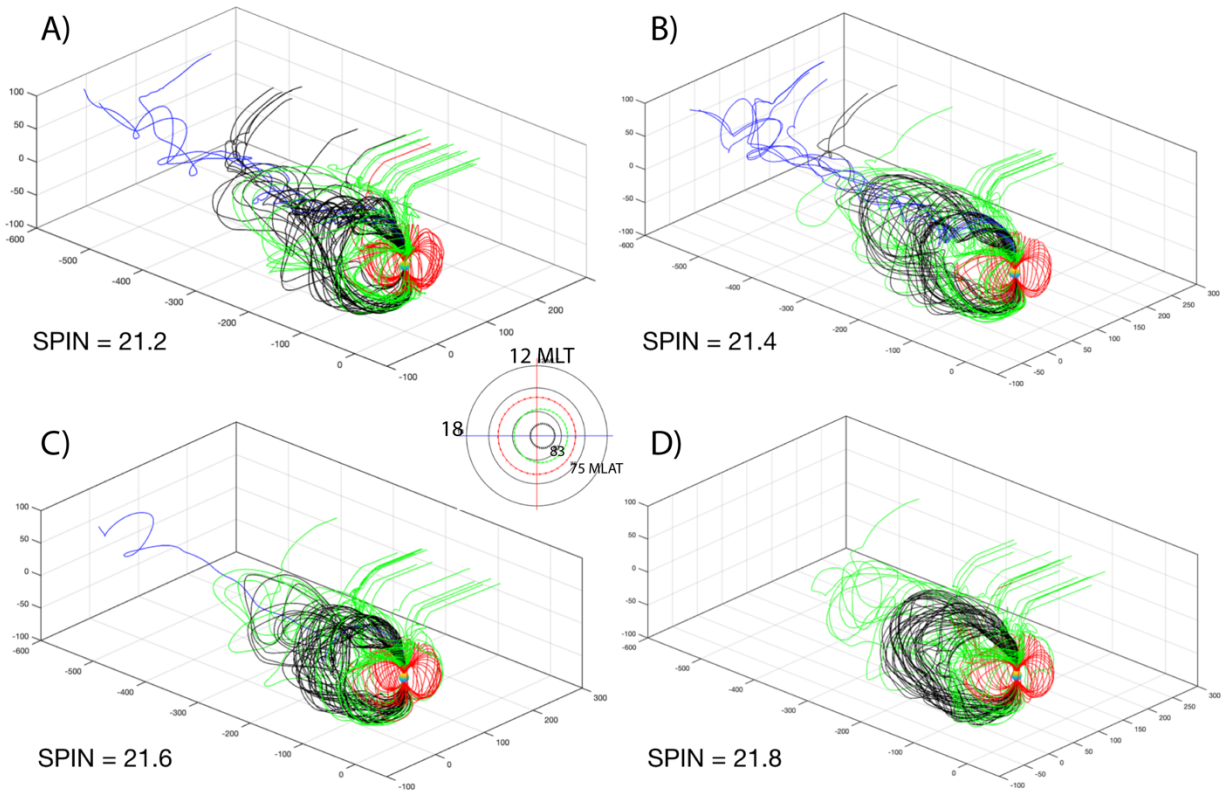

Fig. S6. Instantaneous magnetic field lines derived from different phase of the simulated jovian spin 21. A) spin = 21.2, B) spin = 21.4, C) spin = 21.6 and D) spin = 21.8. The ionospheric footpoint of the field lines are shown in the middle panel of the figure.

REFERENCES AND NOTES

1. D. Grodent, J. T. Clarke, J. H. Waite Jr., S. W. H. Cowley, J.-C. Gérard, J. Kim, Jupiter's polar auroral emissions. *J. Geophys. Res. Space Physics* **108**, 1366 (2003).

2. J. D. Nichols, J. T. Clarke, J. C. Gérard, D. Grodent, K. C. Hansen, Variation of different components of Jupiter's auroral emission. *J. Geophys. Res. Space Physics* **114**, A06210 (2009).

3. B. Bonfond, M. F. Vogt, J.-C. Gérard, D. Grodent, A. Radioti, V. Coumans, Quasi-periodic polar flares at Jupiter: A signature of pulsed dayside reconnections? *Geophys. Res. Lett.* **38**, L02104 (2011).

4. D. Grodent, J. T. Clarke, J. Kim, J. H. Waite Jr., S. W. H. Cowley, Jupiter's main auroral oval observed with HST-STIS. *J. Geophys. Res. Space Physics* **108**, 1389 (2003).

5. T. S. Stallard, S. Miller, S. W. H. Cowley, E. J. Bunce, Jupiter's polar ionospheric flows: Measured intensity and velocity variations poleward of the main auroral oval. *Geophys. Res. Lett.* **30**, 1221 (2003).

6. T. Stallard, S. Miller, G. Millward, R. D. Joseph, On the dynamics of the jovian ionosphere and thermosphere: I. The measurement of ion winds. *Icarus* **154**, 475–491 (2001).

7. L. R. Lyons, Magnetospheric processes leading to precipitation. *Space Sci. Rev.* **80**, 109–132 (1997).

8. G. Paschmann, S. Haaland, R. Treumann, *Auroral Plasma Physics* (Springer Science & Business Media, 2012), vol. 15.

9. J. W. Dungey, Interplanetary magnetic field and the auroral zones. *Phys. Rev. Lett.* **6**, 47–48 (1961).

10. L. C. Evans, E. C. Stone, Electron polar cap and the boundary of open geomagnetic field lines. *J. Geophys. Res.* **77**, 5580–5584 (1972).

11. Y. I. Feldstein, G. V. Starkov, The auroral oval and the boundary of closed field lines of geomagnetic field. *Planet. Space Sci.* **18**, 501–508 (1970).

12. P. T. Newell, T. Sotirelis, S. Wing, Diffuse, monoenergetic, and broadband aurora: The global precipitation budget. *J. Geophys. Res. Space Physics* **114**, A09207 (2009).

13. T. W. Hill, The Jovian auroral oval. *J. Geophys. Res. Space Physics* **106**, 8101–8107 (2001).

14. S. W. H. Cowley, E. J. Bunce, Origin of the main auroral oval in Jupiter's coupled magnetosphere–ionosphere system. *Planet. Space Sci.* **49**, 1067–1088 (2001).

15. B. H. Mauk, D. K. Haggerty, C. Paranicas, G. Clark, P. Kollmann, A. M. Rymer, D. G. Mitchell, S. J. Bolton, S. M. Levin, A. Adriani, F. Allegrini, F. Bagenal, J. E. P. Connerney, G. R. Gladstone, W. S. Kurth, D. J. McComas, D. Ranquist, J. R. Szalay, P. Valek, Juno observations of energetic charged particles over Jupiter's polar regions: Analysis of monodirectional and bidirectional electron beams. *Geophys. Res. Lett.* **44**, 4410–4418 (2017).

16. G. Branduardi-Raymont, A. Bhardwaj, R. F. Elsner, G. R. Gladstone, G. Ramsay, P. Rodriguez, R. Soria, J. H. Waite Jr, T. E. Cravens, A study of Jupiter's aurorae with XMM-Newton. *Astron. Astrophys.* **463**, 761–774 (2007).

17. G. Clark, B. H. Mauk, D. Haggerty, C. Paranicas, P. Kollmann, A. Rymer, E. J. Bunce, S. W. H. Cowley, D. G. Mitchell, G. Provan, R. W. Ebert, F. Allegrini, F. Bagenal, S. Bolton, J. Connerney, S. Kotsiaros, W. S. Kurth, S. Levin, D. J. McComas, J. Saur, P. Valek, Energetic particle signatures of magnetic field-aligned potentials over Jupiter's polar regions. *Geophys. Res. Lett.* **44**, 8703–8711 (2017).

18. R. F. Elsner, N. Lugaz, J. H. Waite Jr, T. E. Cravens, G. R. Gladstone, P. Ford, D. Grodent, A. Bhardwaj, R. J. MacDowall, M. D. Desch, T. Majeed, Simultaneous Chandra X ray, Hubble Space Telescope ultraviolet, and Ulysses radio observations of Jupiter's aurora. *J. Geophys. Res. Space Physics* **110**, A01207 (2005).

19. D. K. Haggerty, B. H. Mauk, C. P. Paranicas, G. Clark, P. Kollmann, A. M. Rymer, S. J. Bolton, J. E. P. Connerney, S. M. Levin, Juno/JEDI observations of 0.01 to >10 MeV energetic ions in the Jovian auroral regions: Anticipating a source for polar X-ray emission. *Geophys. Res. Lett.* **44**, 6476–6482 (2017).

20. D. J. Gershman, G. A. DiBraccio, J. E. P. Connerney, G. Hospodarsky, W. S. Kurth, R. W. Ebert, J. R. Szalay, R. J. Wilson, F. Allegrini, P. Valek, D. J. McComas, F. Bagenal, S. Levin, S. J. Bolton, Juno observations of large-scale compressions of Jupiter's dawnside magnetopause. *Geophys. Res. Lett.* **44**, 7559–7568 (2017).

21. R. W. Ebert, F. Allegrini, F. Bagenal, S. J. Bolton, J. E. P. Connerney, G. Clark, G. A. DiBraccio, D. J. Gershman, W. S. Kurth, S. Levin, P. Louarn, B. H. Mauk, D. J. McComas, M. Reno, J. R. Szalay, M. F. Thomsen, P. Valek, S. Weidner, R. J. Wilson, Accelerated flows at Jupiter's magnetopause: Evidence for magnetic reconnection along the dawn flank. *Geophys. Res. Lett.* **44**, 4401–4409 (2017).

22. M. Desroche, F. Bagenal, P. A. Delamere, N. Erkaev, Conditions at the expanded Jovian magnetopause and implications for the solar wind interaction. *J. Geophys. Res. Space Physics* **117**, A07202 (2012).

23. A. Masters, Model-based assessments of magnetic reconnection and Kelvin-Helmholtz instability at Jupiter's magnetopause. *J. Geophys. Res. Space Physics* **122**, 11,154–11,174 (2017).

24. P. A. Delamere, F. Bagenal, Solar wind interaction with Jupiter's magnetosphere. *J. Geophys. Res. Space Physics* **115**, A10201 (2010).

25. P. A. Delamere, F. Bagenal, Magnetotail structure of the giant magnetospheres: Implications of the viscous interaction with the solar wind. *J. Geophys. Res. Space Physics* **118**, 7045–7053 (2013).

26. E. Chané, J. Saur, S. Poedts, Modeling Jupiter's magnetosphere: Influence of the internal sources. *J. Geophys. Res. Space Physics* **118**, 2157–2172 (2013).

27. T. Ogino, R. J. Walker, M. G. Kivelson, A global magnetohydrodynamic simulation of the Jovian magnetosphere. *J. Geophys. Res. Space Physics* **103**, 225–235 (1998).

28. Y. Sarkango, X. Jia, G. Toth, Global MHD simulations of the response of Jupiter's magnetosphere and ionosphere to changes in the solar wind and IMF. *J. Geophys. Res. Space Physics* **124**, 5317–5341 (2019).

29. R. J. Walker, T. Ogino, M. G. Kivelson, Magnetohydrodynamic simulations of the effects of the solar wind on the Jovian magnetosphere. *Planet. Space Sci.* **49**, 237–245 (2001).

30. Y. Wang, X. Guo, B. Tang, W. Li, C. Wang, Modeling the Jovian magnetosphere under an antiparallel interplanetary magnetic field from a global MHD simulation. *Earth Planet. Phys.* **2**, 303–309 (2018).

31. B. Zhang, P. A. Delamere, X. Ma, B. Burkholder, M. Wiltberger, J. G. Lyon, V. G. Merkin, K. A. Sorathia, Asymmetric Kelvin-Helmholtz instability at Jupiter's magnetopause boundary: Implications for corotation-dominated systems. *Geophys. Res. Lett.* **45**, 56–63 (2018).

32. B. Z. Zhang, K. A. Sorathia, J. G. Lyon, V. G. Merkin, J. S. Garretson, M. Wiltberger, GAMERA: A three-dimensional finite-volume MHD solver for non-orthogonal curvilinear geometries. *Astrophys. J. Suppl. Ser.* **244**, 20 (2019).

33. F. Bagenal, P. A. Delamere, Flow of mass and energy in the magnetospheres of Jupiter and Saturn. *J. Geophys. Res. Space Physics* **116**, A05209 (2011).

34. J. E. Ouellette, B. N. Rogers, M. Wiltberger, J. G. Lyon, Magnetic reconnection at the dayside magnetopause in global Lyon-Fedder-Mobarry simulations. *J. Geophys. Res. Space Physics* **115**, A08222 (2010).

35. J. D. Nichols, S. W. H. Cowley, D. J. McComas, Magnetopause reconnection rate estimates for Jupiter's magnetosphere based on interplanetary measurements at ~5AU. *Ann. Geophys.* **24**, 393–406 (2006).

36. M. F. Vogt, M. G. Kivelson, K. K. Khurana, R. J. Walker, B. Bonfond, D. Grodent, A. Radioti, Improved mapping of Jupiter's auroral features to magnetospheric sources. *J. Geophys. Res. Space Physics* **116**, A03220 (2011).

37. B. G. Swithenbank-Harris, J. D. Nichols, E. J. Bunce, Jupiter's dark polar region as observed by the Hubble space telescope during the Juno approach phase. *J. Geophys. Res. Space Physics* **124**, 9094–9105 (2019).

38. T. S. Stallard, J. T. Clarke, H. Melin, S. Miller, J. D. Nichols, J. O'Donoghue, R. E. Johnson, J. E. P. Connerney, T. Satoh, M. Perry, Stability within Jupiter's polar auroral 'Swirl region' over moderate timescales. *Icarus* **268**, 145–155 (2016).

39. T. S. Stallard, S. Miller, L. M. Trafton, T. R. Geballe, R. D. Joseph, Ion winds in Saturn's southern auroral/polar region. *Icarus* **167**, 204–211 (2004).

40. R. E. Johnson, T. S. Stallard, H. Melin, J. D. Nichols, S. W. H. Cowley, Jupiter's polar ionospheric flows: High resolution mapping of spectral intensity and line-of-sight velocity of H_3^+ ions. *J. Geophys. Res. Space Physics* **122**, 7599–7618 (2017).

41. W. Lotko, R. H. Smith, B. Z. Zhang, J. E. Ouellette, O. J. Brambles, J. G. Lyon, Ionospheric control of magnetotail reconnection. *Science* **345**, 184–187 (2014).

42. R. E. Johnson, H. Melin, T. S. Stallard, C. Tao, J. D. Nichols, M. N. Chowdhury, Mapping H_3^+ temperatures in Jupiter's Northern auroral ionosphere using VLT-CRIRES. *J. Geophys. Res. Space Physics* **123**, 5990–6008 (2018).

43. S. E. Milan, E. J. Bunce, S. W. H. Cowley, C. M. Jackman, Implications of rapid planetary rotation for the Dungey magnetotail of Saturn. *J. Geophys. Res. Space Physics* **110**, A03209 (2005).

44. J. Isbell, A. J. Dessler, J. H. Waite Jr, Magnetospheric energization by interaction between planetary spin and the solar wind. *J. Geophys. Res. Space Physics* **89**, 10716–10722 (1984).

45. W. S. Kurth, J. D. Sullivan, D. A. Gurnett, F. L. Scarf, H. S. Bridge, E. C. Sittler Jr, Observations of Jupiter's distant magnetotail and wake. *J. Geophys. Res. Space Physics* **87**, 10373–10383 (1982).

46. T. S. Stallard, K. H. Baines, H. Melin, T. J. Bradley, L. Moore, J. O'Donoghue, S. Miller, M. N. Chowdhury, S. V. Badman, H. J. Allison, E. Roussos, Local-time averaged maps of H_3^+ emission, temperature and ion winds. *Philos. Trans. Royal Soc. A* **377**, 20180405 (2019).

47. T. Miyoshi, K. Kusano, A global MHD simulation of the Jovian magnetosphere interacting with/without the interplanetary magnetic field. *J. Geophys. Res. Space Physics* **106**, 10723–10742 (2001).

48. T. Moriguchi, A. Nakamizo, T. Tanaka, T. Obara, H. Shimazu, Current systems in the Jovian magnetosphere. *J. Geophys. Res. Space Physics* **113**, (2008).

49. B. U. Ö. Sonnerup, Theory of the low-latitude boundary layer. *J. Geophys. Res. Space Physics* **85**, 2017–2026 (1980).

50. A. Keiling, J. R. Wygant, C. A. Cattell, F. S. Mozer, C. T. Russell, The global morphology of wave poynting flux: Powering the aurora. *Science* **299**, 383–386 (2003).

51. D. Grodent, A brief review of ultraviolet auroral emissions on giant planets. *Space Sci. Rev.* **187**, 23–50 (2015).

52. O. J. Brambles, W. Lotko, B. Zhang, M. Wiltberger, J. Lyon, R. J. Strangeway, Magnetosphere sawtooth oscillations induced by ionospheric outflow. *Science* **332**, 1183–1186 (2011).

53. M. Wiltberger, W. Lotko, J. G. Lyon, P. Damiano, V. Merkin, Influence of cusp O^+ outflow on magnetotail dynamics in a multifluid MHD model of the magnetosphere. *J. Geophys. Res. Space Phys.* **115**, A00J05 (2010).

54. J. G. Lyon, J. A. Fedder, C. M. Mobarry, The Lyon-Fedder-Mobarry (LFM) global MHD magnetospheric simulation code. *J. Atmos. Sol. Terr. Phys.* **66**, 1333–1350 (2004).

55. B. Zhang, O. J. Brambles, P. A. Cassak, J. E. Ouellette, M. Wiltberger, W. Lotko, J. G. Lyon, Transition from global to local control of dayside reconnection from ionospheric-sourced mass loading. *J. Geophys. Res. Space Phys.* **122**, 9474–9488 (2017).

56. J. E. Ouellette, O. J. Brambles, J. G. Lyon, W. Lotko, B. N. Rogers, Properties of outflow-driven sawtooth substorms. *J. Geophys. Res. Space Physics* **118**, 3223–3232 (2013).

57. R. H. Varney, M. Wiltberger, B. Zhang, W. Lotko, J. Lyon, Influence of ion outflow in coupled geospace simulations: 1. Physics-based ion outflow model development and sensitivity study. *J. Geophys. Res. Space Phys.* **121**, 9671–9687 (2016).

58. V. G. Merkin, J. G. Lyon, Effects of the low-latitude ionospheric boundary condition on the global magnetosphere. *J. Geophys. Res. Space Phys.* **115**, A10202 (2010).

59. L. C. Ray, R. E. Ergun, P. A. Delamere, F. Bagenal, Magnetosphere-ionosphere coupling at Jupiter: A parameter space study. *J. Geophys. Res. Space Physics* **117**, A01205 (2012).

60. S. V. Badman, S. W. H. Cowley, Significance of Dungey-cycle flows in Jupiter's and Saturn's magnetospheres, and their identification on closed equatorial field lines. *Ann. Geophys.* **25**, 941–951 (2007).

61. C. M. Komar, P. A. Cassak, J. C. Dorelli, A. Glocer, M. M. Kuznetsova, Tracing magnetic separators and their dependence on IMF clock angle in global magnetospheric simulations. *J. Geophys. Res. Space Physics* **118**, 4998–5007 (2013).

62. R. E. Lopez, R. Bruntz, E. J. Mitchell, M. Wiltberger, J. G. Lyon, V. G. Merkin, Role of magnetosheath force balance in regulating the dayside reconnection potential. *J. Geophys. Res. Space Phys.* **115**, A12216 (2010).

63. O. J. Brambles, W. Lotko, P. A. Damiano, B. Zhang, M. Wiltberger, J. Lyon, Effects of causally driven cusp O^+ outflow on the storm time magnetosphere-ionosphere system using a multifluid global simulation. *J. Geophys. Res. Space Phys.* **115**, A00J04 (2010).

64. R. E. Lopez, The integrated dayside merging rate is controlled primarily by the solar wind. *J. Geophys. Res. Space Physics* **121**, 4435–4445 (2016).